Tool path generation for chamfering drill holes of a pipe with constant width

Takato Sato [a], Youichi Sato [b], Takashi Maekawa [a,*]

[a] *Department of Mechanical Engineering, Yokohama National University, Japan*
[b] *Xebec Technology, Japan*

A R T I C L E   I N F O

A B S T R A C T

When drilling circular holes into metal circular pipes, burr is generated at the hole entrance as well as at the hole exit. The burrs generated at the edge curves associated with the outer and inner pipe surfaces must be removed by constant chamfering. Geometrically, the two edge curves can be defined as cylinder-to-pipe intersection curves. In this paper, we employ differential geometric properties of the surface-to-surface intersection curves in order to generate an interference-free tool path with constant chamfering for a ball-end cutter. We demonstrate the effectiveness of our method by conducting experiments with physical pipe models.

© 2016 Elsevier Ltd. All rights reserved.

1. Introduction

Burr is formed as a result of the undesirable plastic flow of metals through various machining operations applied to tasks such as grinding, drilling, milling, engraving, and turning [1]. Burr may cause injury to workers during the assembly process, and may trigger severe problems in high-speed equipment, fluid-power systems, food processing, etc. [1]. Therefore, deburring must be included in the finishing process not only to remove the unwanted burr, but also to ensure uniform chamfering at the produced edges for aesthetic purposes. It is also known that constant chamfering can greatly improve the performance and lifetime of products [1]. Unfortunately, the most common burr removal process currently employed in manufacturing plants is hand deburring using hand-held deburring tools, which is time consuming [1]. Furthermore, there is no chamfer on the curved edge. According to Gillespie [2], for precision parts, edge finishing frequently constitutes 30% of the overall cost. Liao et al. [3] proposed the modeling and control of an automated polishing/deburring process that utilizes a dual-purpose compliant toolhead. However, the problem of tools interfering with work was not discussed. Song and Song [4] studied a tool path modification method using an iterative closest point (ICP) based contour matching algorithm to enable the robotic deburring process to compensate for the position/orientation

errors of the workpiece when it is placed in a jig. The proposed method was implemented on a six degree of freedom (DOF) articulated manipulator with force control strategies and a virtual wall to perform the robotic deburring. However, the quality of the deburring was not discussed.

In this paper, we introduce an interference-free automatic tool path generation method for a ball-end cutter with constant chamfering to remove burrs resulting from the drilling of a circular pipe based on the differential geometry of cylinder-to-pipe intersection curves. As shown in Fig. 2(a), the resulting intersection curve is a space curve, which looks like the curved edge of a potato chip. We assume that the drilling operation is perpendicular to the pipe without eccentricity, and a tool consists of a ball-end cutter and a circular rod, which must not interfere with the pipe, with the exception of the cutter contact point, while deburring.

The remaining part of this paper is organized as follows. In Section 2, we present the differential geometry of the cylinder-to-pipe intersection curves. The tool path generation for the deburring process is discussed in Section 3. In Section 4, we study cutter interference avoidance. In Section 5, we demonstrate the effectiveness of our method by conducting experiments using physical pipe models. Finally, we conclude the paper in Section 6.

2. Differential geometry of cylinder-to-pipe intersection curves

We first introduce several notations and definitions. Bold letters such as $\mathbf{t}$, $\mathbf{C}(\theta)$ denote vectors and vector functions. Equivalently, (a, b, c) and $(a(\theta), \quad b(\theta), \quad c(\theta))$ denote vectors and vector functions, respectively. The dot $\dot{\mathbf{C}}(\theta)$ denotes the differentiation of $\mathbf{C}(\theta)$ with respect to the parameter θ.

* Corresponding author. Tel.: +81 45 339 3930.
  E-mail address: maekawa@ynu.ac.jp (T. Maekawa).
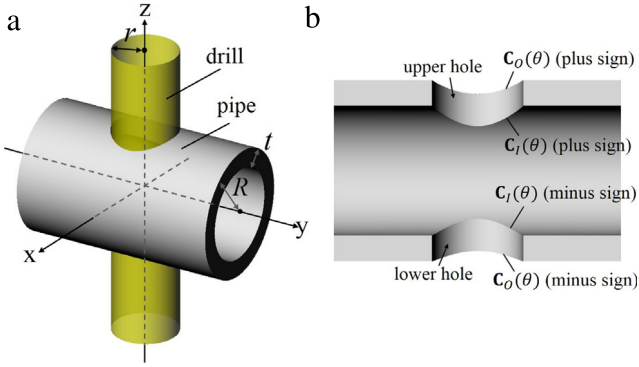
Fig. 1. (a) A drill (cylinder) intersects a circular pipe orthogonally without eccentricity. (b) Four intersection curves.
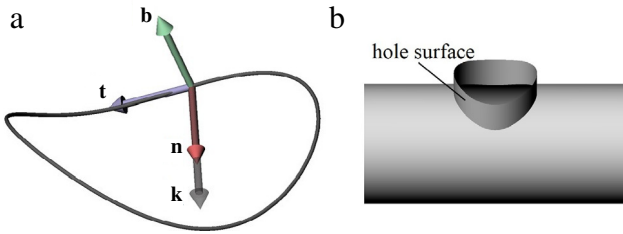
Fig. 2. Cylinder-to-pipe intersection: (a) Frenet frame along the intersection curve. The intersection curve looks like the edge of a potato chip. (b) The hole surface spanned by the two intersection curves is a ruled surface.

2.1. Cylinder-to-pipe intersection curve

Let us define a mathematical description of the geometry, which is illustrated in Fig. 1(a). In this paper, we consider the geometry of a cylinder-to-pipe intersection where a circular pipe consisting of outer and inner surfaces with thickness t are intersected orthogonally without eccentricity by a circular cylinder representing a drill. In other words, the center lines of the pipe and drill intersect orthogonally. We assume that the drill is represented by a cylinder having a radius r, and its centerline coincides with the z-axis. It can be expressed by a parametric form:

$$\mathbf{D}(\theta, z) = (r \cos \theta, \ r \sin \theta, \ z), \tag{1}$$

where θ is the parameter within $0 \leq \theta \leq 2\pi$. We take the center line of the outer pipe surface, which is coincident with the y-axis, having a radius R, and represent it by an implicit form:

$$x^2 + z^2 = R^2. \tag{2}$$

Similarly, the inner pipe surface is given by

$$x^2 + z^2 = R_I^2, \tag{3}$$

where $R_I = R - t$ is the radius of inner pipe surface and t is the pipe thickness. We can obtain the intersection curves $\mathbf{C}_O(\theta)$ between the drill surface and the outer pipe surface by substituting the vector components of (1) into (2), and solving for z, which yields a parametric representation of the intersection curve [5,6]:

$$\mathbf{C}_O(\theta) = \left(r \cos \theta, \ r \sin \theta, \ \pm \sqrt{R^2 - r^2 \cos^2 \theta} \right), \tag{4}$$

where the plus sign corresponds to the upper intersection curve, while the minus sign corresponds to the lower intersection curve (see Fig. 1(b)). In this paper, we only consider the upper intersection curve (plus sign), as the minus sign can be obtained in the same manner. Similarly, we have two intersection curves $\mathbf{C}_I(\theta)$ for the inner pipe surface:

$$\mathbf{C}_I(\theta) = \left(r \cos \theta, r \sin \theta, \pm \sqrt{R_I^2 - r^2 \cos^2 \theta} \right), \tag{5}$$
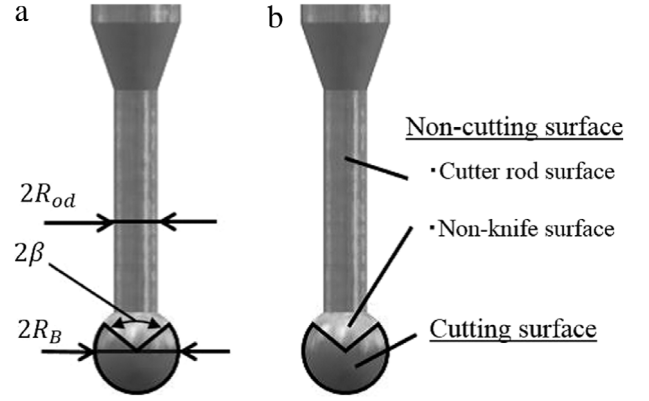
Fig. 3. Ball-end cutter: (a) Geometry. (b) Classification of the ball-end cutter surface.

where we only consider the upper intersection curve (plus sign) (see Fig. 1(b)). To simplify the notation, we drop the subscripts O, I from $\mathbf{C}$ throughout the rest of the paper, except when stated otherwise.

2.2. Differential geometry of intersection curve

The unit tangent $\mathbf{t}$, binormal $\mathbf{b}$, and normal $\mathbf{n}$ vectors of the intersection curve $\mathbf{C}(\theta)$ (see Fig. 2(a)) can be obtained as

$$\mathbf{t} = \frac{\dot{\mathbf{C}}(\theta)}{|\dot{\mathbf{C}}(\theta)|}, \tag{6}$$

$$\mathbf{b} = \frac{\dot{\mathbf{C}}(\theta) \times \ddot{\mathbf{C}}(\theta)}{|\dot{\mathbf{C}}(\theta) \times \ddot{\mathbf{C}}(\theta)|}, \tag{7}$$

$$\mathbf{n} = \mathbf{b} \times \mathbf{t}. \tag{8}$$

The curvature of the intersection curve is given by

$$\kappa = \frac{|\dot{\mathbf{C}}(\theta) \times \ddot{\mathbf{C}}(\theta)|}{|\dot{\mathbf{C}}(\theta)|^3}, \tag{9}$$

and the curvature vector $\mathbf{k}$ is obtained as

$$\mathbf{k} = \kappa \mathbf{n}. \tag{10}$$

3. Tool path generation

3.1. Hole surface

The hole surface $\mathbf{H}(\theta, \tau)$ (see Fig. 2(b)) is a ruled surface bounded by two intersection curves $\mathbf{C}_I(\theta)$ and $\mathbf{C}_O(\theta)$, and is defined as follows:

$$\mathbf{H}(\theta, \tau) = (1 - \tau)\mathbf{C}_I(\theta) + \tau \mathbf{C}_O(\theta). \tag{11}$$

The unit normal vector of the hole surface $\mathbf{N}_H$ is simply a unit normal of a cross-sectional circle of the cylinder representing the drill, and it is given by

$$\mathbf{N}_H = (\cos \theta, \ \sin \theta, \ 0). \tag{12}$$

3.2. Ball-end cutter

The deburring cutter consists of double-start knife edges wrapped around a sphere of diameter $2R_B$ in the form of a right-handed helix with a lead angle 15°, and it is connected to a rod of diameter $2R_{od}$, as illustrated in Fig. 3(a). The knife edge of the cutter is limited to the angle $360° - 2\beta$, as depicted in Fig. 3(a). The non-cutting surface consists of the non-knife and cutter rod surfaces, as illustrated in Fig. 3(b). The ball-end cutter is attached to a compact machining center (DMG Mori Seiki MILLTAP 700) that is equipped with a vertical 3-axis milling.
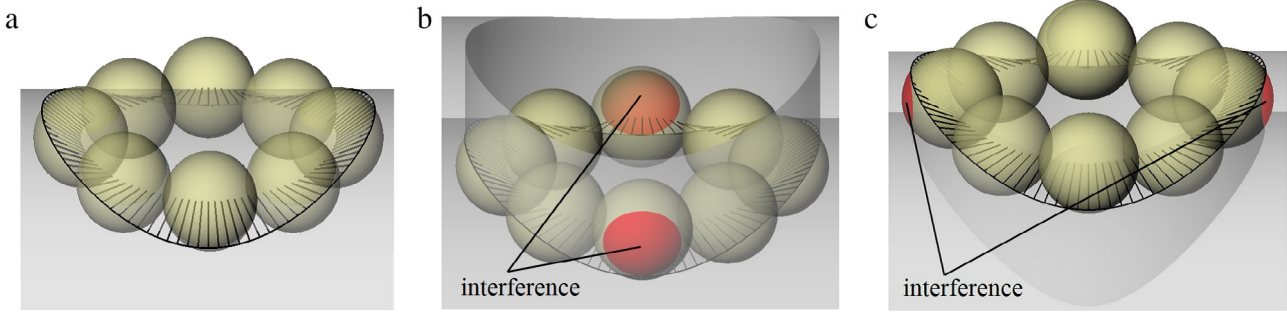
Fig. 4. Global cutter interference: (a) Ideal path with curvature plot in black. (b) Interference while deburring $\mathbf{C}_I$, where the red portion indicates the interference regions. (c) Interference while deburring $\mathbf{C}_O$, where the red portion indicates the interference regions. (For interpretation of the references to color in this figure legend, the reader is referred to the web version of this article.)
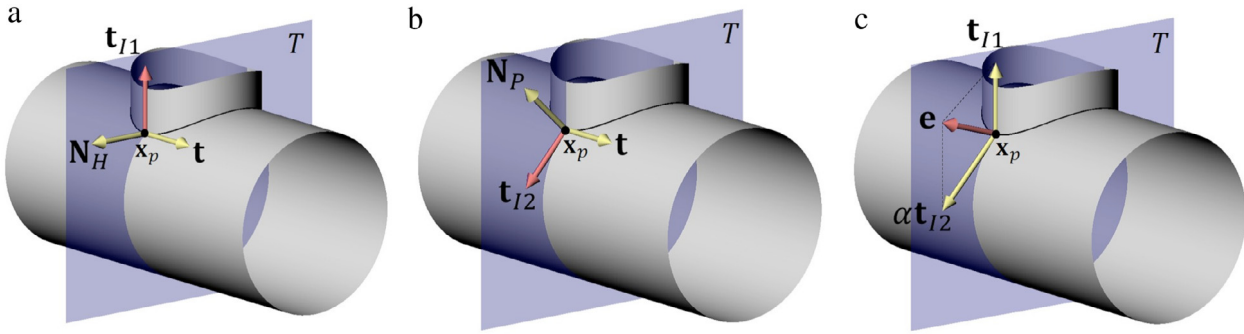
Fig. 5. (a) Unit tangent vector $\mathbf{t}_{I1}$ of the intersection curve between plane T and the hole surface. (b) Unit tangent vector $\mathbf{t}_{I2}$ of the intersection curve between plane T and the pipe inner surface. (c) The unit vector $\mathbf{e}$ pointing from the center of the cutter to the cutter contact point.

3.3. Cutter location

The cutter location is defined as the coordinates of the center of the ball-end cutter. Ideally, it should be along the offset curve of the intersection curve $\mathbf{C}(\theta)$ with an offset distance R_B [7,8] considering initially the case of zero width chamfering, as illustrated in Fig. 4(a). However, the ball-end cutter collides with the hole surface when deburring the inner/outer intersection curve $\mathbf{C}_I/\mathbf{C}_O$, if the vector from the cutter contact point to the center of the ball-end cutter has a positive/negative z component respectively, as illustrated in Fig. 4(b)/(c), respectively. In the rest of the paper, we only consider the case for the inner intersection curve as the outer intersection curve case is similar. In order to avoid such collisions, we attempt to set the cutter location on the normal plane T (similar to the offset curve), which is orthogonal to the tangent vector $\mathbf{t}$ of the intersection curve at the reference point $\mathbf{x}_p = \mathbf{C}_I(\theta)$ (see Fig. 5). The equation for plane T is given by:

$$ax + by + cz + d = 0, \tag{13}$$

where $(a, b, c) = \mathbf{t}$ and $d = -\mathbf{t} \cdot \mathbf{x}_p$. Let us define the unit tangent vector $\mathbf{t}_{I1}$ (see Fig. 5(a)) of the intersection curve between plane T and the hole surface (11) as follows:

$$\mathbf{t}_{I1} = \mathbf{N}_H \times \mathbf{t}. \tag{14}$$

We also define the unit tangent vector $\mathbf{t}_{I2}$ (see Fig. 5(b)) of the intersection curve between the inner pipe surface and plane T as follows:

$$\mathbf{t}_{I2} = \mathbf{t} \times \mathbf{N}_P, \tag{15}$$

where $\mathbf{N}_P$ is a unit normal vector of the inner pipe surface, and can be obtained using the implicit expression of the inner pipe surface $f_P(x, y, z) = x^2 + z^2 - R_I^2 = 0$ leading to

$$\mathbf{N}_P = \frac{\nabla f_P}{|\nabla f_P|} = \left(\frac{x}{\sqrt{x^2 + z^2}}, \ 0, \ \frac{z}{\sqrt{x^2 + z^2}} \right). \tag{16}$$

Substituting the parametric expression (5) into (16) yields

$$\mathbf{N}_P = \left(\frac{r \cos \theta}{R_I}, \ 0, \ \frac{\sqrt{R_I^2 - r^2 \cos^2 \theta}}{R_I} \right). \tag{17}$$

Because our goal is to generate the constant chamfering without any interference, it is natural to set the cutter location along the bisection vector of $\mathbf{t}_{I1}$ and $\mathbf{t}_{I2}$, as shown in Fig. 6(a). Therefore, the unit vector pointing from the center of the cutter towards the cutter contact point (see Fig. 5(c)) is given by:

$$\mathbf{e} = \frac{\mathbf{t}_{I1} + \alpha \mathbf{t}_{I2}}{|\mathbf{t}_{I1} + \alpha \mathbf{t}_{I2}|}. \tag{18}$$

We refer to the unit vector $-\mathbf{e}$ as the cutter vector. When $\alpha = 1$, $\mathbf{e}$ is a bisector of an angle spanned by $\mathbf{t}_{I1}$ and $\mathbf{t}_{I2}$ (see Fig. 6(a)). In general, α is set to be equal to 1; however, in some situations, α is adjusted to avoid cutter rod interference (see Section 4.2). If we denote the feed of the tool towards the pipe as δ, the cutter location $\mathbf{C}_L(\theta) = (x_{CL}(\theta), \ y_{CL}(\theta), \ z_{CL}(\theta))$ is given by

$$\mathbf{C}_L(\theta) = \mathbf{x}_p - (R_B - \delta)\mathbf{e}, \tag{19}$$

as shown in Fig. 6(a), and hence the equation of the ball-end cutter, which is represented as a sphere, can be expressed as:

$$|\mathbf{x} - \mathbf{C}_L(\theta)|^2 = R_B^2, \tag{20}$$

where $\mathbf{x} = (x, y, z)$. As illustrated in Fig. 6(b), the chamfering width W can be defined as the line between points A and B. Point A can be obtained as an intersection point between the straight line emanating from $\mathbf{x}_p$ along the vector $\mathbf{t}_{I1}$:

$$\mathbf{r}_1(\zeta) = \mathbf{x}_p + \zeta \mathbf{t}_{I1}, \tag{21}$$

and the sphere (20). Substituting $\mathbf{r}_1(\zeta)$ into $\mathbf{x}$ of (20) results in the following quadratic equation:

$$\zeta^2 + 2(R_B - \delta)\mathbf{e} \cdot \mathbf{t}_{I1}\zeta + \delta^2 - 2\delta R_B = 0, \tag{22}$$
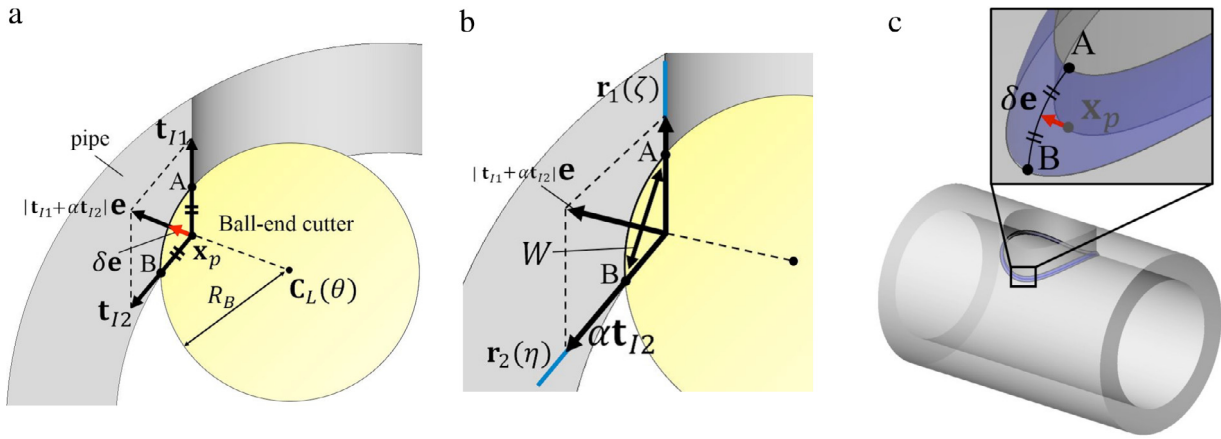
Fig. 6. Chamfering width W: (a) Bisection of $\mathbf{t}_{I1}$ and $\mathbf{t}_{I2}$ ($\alpha = 1$). (b) Cross section of the chamfering when $\alpha \neq 1$. (c) Three orbits of point A, point B, and $\mathbf{x}_p$, and close-up view.
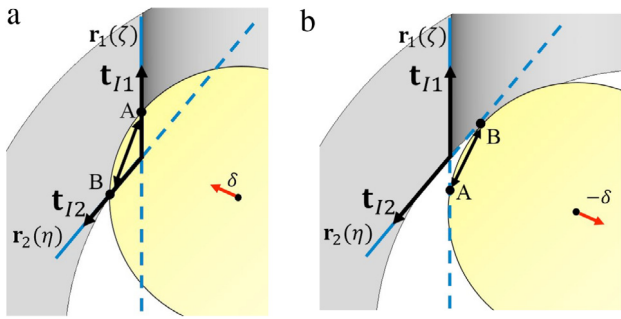
Fig. 7. Solution of Newton's method. (a) Meaningful solution. (b) Unwanted solution.

Fig. 8. Chordal deviation of the approximated line segment: (a) Initial equi-length line segments (e.g., number of line segments: 12). (b) Line segments are subdivided if the chordal deviation is not within the tolerance.

where the meaningful solution is

$$\zeta = -(R_B - \delta)\mathbf{e} \cdot \mathbf{t}_{I1} + \sqrt{(R_B - \delta)^2(\mathbf{e} \cdot \mathbf{t}_{I1})^2 - (\delta^2 - 2\delta R_B)}. \quad (23)$$

Similarly, point B can be obtained as an intersection point between the line along $\mathbf{t}_{I2}$:

$$\mathbf{r}_2(\eta) = \mathbf{x}_p + \eta \mathbf{t}_{I2}, \quad (24)$$

and the sphere. The meaningful solution is

$$\eta = -(R_B - \delta)\mathbf{e} \cdot \mathbf{t}_{I2} + \sqrt{(R_B - \delta)^2(\mathbf{e} \cdot \mathbf{t}_{I2})^2 - (\delta^2 - 2\delta R_B)}. \quad (25)$$

Because ζ and η are both functions of δ, the chamfering width W can be expressed as a function of δ:

$$W(\delta) = |\mathbf{r}_1(\zeta(\delta)) - \mathbf{r}_2(\eta(\delta))|. \quad (26)$$

Thus, given the chamfering width W, the feed of the tool δ can be obtained by finding the root for

$$G(\delta) = |\mathbf{r}_1(\zeta(\delta)) - \mathbf{r}_2(\eta(\delta))|^2 - W^2 = 0. \quad (27)$$

We employed Newton's method to find the root of (27), where we used a small positive number $\delta = W/4$ for the initial value. Starting with this initial value, Newton's method converges to the correct solution (see Fig. 7(a)), whereas with a negative small number, it generally converges to the unwanted solution (see Fig. 7(b)). If we use the initial values with a large magnitude, the solution generally diverges.

Fig. 6(c) depicts the three orbits of point A, point B and $\mathbf{x}_p$. We can observe that $\overline{AB}$ is constant and the line segments $\overline{A\mathbf{x}_p}$ and $\overline{B\mathbf{x}_p}$ are of equal length (see Fig. 6(a)). In other words, the cutter vector divides the cross section of the machined surface into two equi-length circular arcs.

3.4. Generation of line segments

The procedure begins with approximating the intersection curve $\mathbf{C}(\theta)$ by a set of equi-length line segments (see Fig. 8(a)). The maximum chordal deviation is calculated for each line segment, and if the deviation is greater than the prescribed tolerance, the curve is subdivided until the chordal deviation is within the tolerance ϵ [9].

Because the intersection curve is not arc length parametrized, points of the curve obtained at parameter values $\theta_0, \theta_1, \dots, \theta_N$ corresponding to a uniform increment $\Delta\theta = \theta_k - \theta_{k-1}$ will not be evenly distributed along the curve. If we denote the arc length of the intersection curve as s, then the parametric speed of the curve, which is the rate of change of its length s with respect to the parameter θ, is given as $v = \frac{ds}{d\theta} = |\dot{\mathbf{C}}(\theta)|$. The total length of the intersection curve L is evaluated as:

$$L = \int_0^{2\pi} ds = \int_0^{2\pi} \frac{ds}{d\theta} d\theta = \int_0^{2\pi} |\dot{\mathbf{C}}(\theta)| d\theta. \quad (28)$$

If we divide the total arc length L by N segments, the length of the divided curve segment Δs is given by

$$\Delta s = \frac{L}{N}. \quad (29)$$

We want to find the parameter θ_k such that

$$k\Delta s = \int_0^{\theta_k} |\dot{\mathbf{C}}(\theta)| d\theta. \quad (30)$$

If we rewrite (30) as

$$f(\theta_k) = \int_0^{\theta_k} |\dot{\mathbf{C}}(\theta)| d\theta - k\Delta s = 0, \quad (31)$$
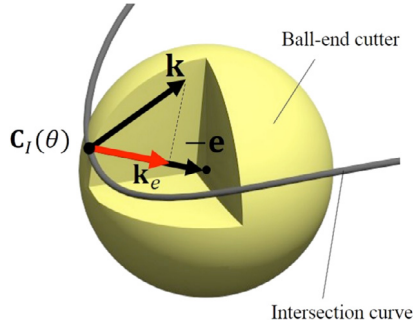
Fig. 9. The condition $R_B \leq 1/|\mathbf{k}_e(\theta)|$ is satisfied; therefore, there is no local interference.

our task is to find the root of $f(\theta_k) = 0$ [10,11]. We use the Gauss–Legendre n-point quadrature formula [12] to evaluate the integral in (31). The root can be obtained using Newton's method as:

$$\theta_k^{(n)} = \theta_k^{(n-1)} - \frac{f(\theta_k^{(n-1)})}{\dot{f}(\theta_k^{(n-1)})}, \tag{32}$$

where the superscript (n) denotes the nth iteration, and

$$\dot{f}(\theta_k^{(n-1)}) = |\dot{\mathbf{C}}(\theta_k^{(n-1)})| = v(\theta_k^{(n-1)}). \tag{33}$$

We approximate the deviation λ by the distance between point $\mathbf{C}\left(\frac{\theta_k+\theta_{k+1}}{2}\right)$ and the line segment connecting $\mathbf{C}(\theta_k)$ and $\mathbf{C}(\theta_{k+1})$, as shown in Fig. 8(b). This leads us to

$$\lambda = \frac{|(\mathbf{C}(\theta_{k+1}) - \mathbf{C}(\theta_k)) \times (\mathbf{C}\left(\frac{\theta_k+\theta_{k+1}}{2}\right) - \mathbf{C}(\theta_k))|}{|\mathbf{C}(\theta_{k+1}) - \mathbf{C}(\theta_k)|}. \tag{34}$$

If the deviation of the linear segment to the curve segment is not within the prescribed tolerance ϵ, we add point $\mathbf{C}\left(\frac{\theta_k+\theta_{k+1}}{2}\right)$ as a new reference point and split the curve segment into two line segments. The number of initial line segments is typically $N = 60$, and hence, the intervals between them are small. Accordingly, there is no significant difference if we take the parametric midpoint or arc length midpoint for adding the new reference points. Therefore, we choose the parametric midpoint for simplicity.

4. Cutter interference avoidance

There are two types of cutter interference, namely, the ball-end cutter interference and the non-cutting surface interference. The ball-end cutter interference can be further divided into a local interference, where the radius of the ball exceeds the local radius of curvature along the path, and the global interference, where the ball-end cutter interferes with the hole surface because of the global distance between them.

4.1. Ball-end cutter interference

4.1.1. Local interference

As shown in Fig. 4(a), ideally, it is best to locate the center of the ball-end cutter along the curvature vector of the intersection curve. In such cases, the condition required to avoid local cutter interference is:

$$R_B \leq \frac{1}{\kappa(\theta)}, \quad (0 \leq \theta \leq 2\pi). \tag{35}$$

However, in real operations, the center of the cutter is located along the cutter vector $-\mathbf{e}$, as discussed in Section 3.3. Therefore,
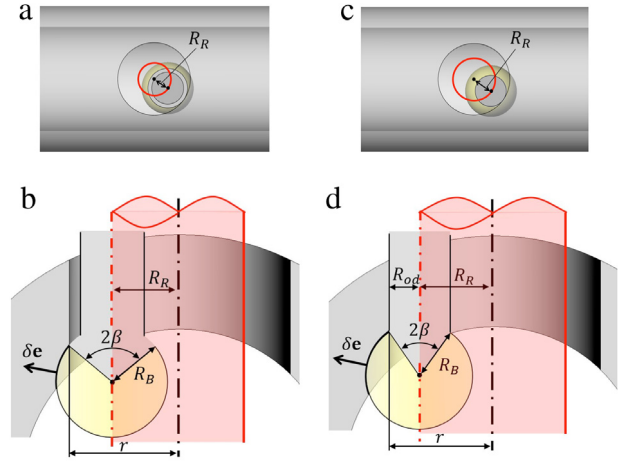
Fig. 10. Cutter rod interference. Figures in the left-hand side column are the cases where the non-knife surface of the cutter makes contact with the hole surface (case (i)), while those in the right-hand side column are the cases where the cutter rod touches the hole surface (case (ii)): (a) Top view. (b) Front view of (a). (c) Top view. (d) Front view of (c).

as shown in Fig. 9, the condition to avoid local cutter interference becomes:

$$R_B \leq \frac{1}{|\mathbf{k}_e(\theta)|}, \quad (0 \leq \theta \leq 2\pi), \tag{36}$$

where

$$\mathbf{k}_e(\theta) = [\mathbf{k}(\theta) \cdot (-\mathbf{e}(\theta))][-\mathbf{e}(\theta)]. \tag{37}$$

4.1.2. Global interference

As illustrated in Fig. 4(b), the ball-end cutter interferes with the hole surface when deburring $\mathbf{C}_I(\theta)$, if the cutter vector $-\mathbf{e}$ has a positive z-component. In order to avoid global cutter interference, we must keep the z-component of the cutter vector as $-e_z \leq 0$. Below, we prove that if $\alpha = 1$ in (18), then $-e_z \leq 0$ for any θ.

Proof. Because the z-component of $\mathbf{t}_{I1}$ and $\mathbf{t}_{I2}$ are given by

$$\mathbf{t}_{I1z} = \frac{\sqrt{R_I^2 - r^2\cos^2\theta}}{\sqrt{R_I^2 - r^2\cos^4\theta}}, \tag{38}$$

$$\mathbf{t}_{I2z} = \frac{-r\cos^2\theta\sqrt{R_I^2 - r^2\cos^2\theta}}{R_I\sqrt{R_I^2 - r^2\cos^4\theta}}, \tag{39}$$

the z-component of $\mathbf{t}_{I1} + \alpha\mathbf{t}_{I2}$, $\bar{e}_z$ becomes

$$\bar{e}_z = \frac{\sqrt{R_I^2 - r^2\cos^2\theta}}{\sqrt{R_I^2 - r^2\cos^4\theta}}\left(1 - \alpha\frac{r}{R_I}\cos^2\theta\right). \tag{40}$$

As $R_I \leq r$, it is easy to find that $-\bar{e}_z \leq 0$ for any θ when $\alpha = 1$, and hence $-e_z \leq 0$. This completes the proof. In case the avoidance of the cutter rod interference is applied, α is not equal to 1. In such cases, α must satisfy

$$\alpha \leq \frac{R_I}{r\cos^2\theta}. \tag{41}$$

4.2. Non-cutting surface interference

As illustrated in Fig. 3, the non-cutting surface consists of the non-knife and cutter rod surfaces. Fig. 10(a) and (b) show case (i) where the non-knife surface (see Fig. 3) of the cutter contacts the hole surface $\mathbf{H}(\theta, \tau)$, while Fig. 10(c) and (d) illustrate
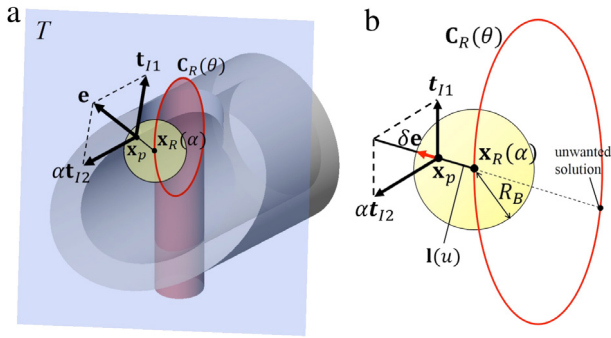
Fig. 11. (a) Determination of α to avoid cutter rod interference. (b) Close-up view of (a). (For interpretation of the references to color in this figure legend, the reader is referred to the web version of this article.)

Fig. 12. (a) Degenerate case ($\theta = \pi/2, 3\pi/2$). (b) Close-up view of (a).

case (ii) where the cutter rod touches the hole surface during the deburring operation. We can treat both cases in a similar manner by considering the non-knife surface of the ball-end cutter as a part of the cutter rod. In other words, it is equivalent to checking interference using a cutter with a larger rod diameter that encompasses the non-cutting region of the ball-end cutter.

Let us define a cylinder (red in Fig. 10) generated by revolving the center line of the cutter rod around the center line of the drill, which defines a non-cutting surface interference-free region. If we denote the radius of the cylinder as R_R, where $R_R = r - R_B \sin \beta$ for case (i), or $R_R = r - R_{od}$ for case (ii), then the cylinder can be expressed as:

$$\mathbf{R}(\theta, z) = (R_R \cos \theta, \ R_R \sin \theta, \ z). \tag{42}$$

To avoid the interference, we adjust α so that the center of the cutter rod axis must stay within the cylinder (42). In other words, the limit cutter location point must be on the intersection curve (red curve in Fig. 11) between the plane (13) and the red cylinder. Therefore, we have:

$$aR_R \cos \theta + bR_R \sin \theta + cz + d = 0. \tag{43}$$

In general, the plane is not parallel to the z-aix, thus $c \neq 0$, and hence the intersection curve between the plane and cylinder can be obtained as:

$$\mathbf{C}_R(\theta) = \left(R_R \cos \theta, R_R \sin \theta, -\frac{aR_R \cos \theta + bR_R \sin \theta + d}{c} \right). \tag{44}$$

Alternatively, we could set $\alpha = 1$ and adjust the chamfering width such that the non-cutting surface does not interfere with the pipe surface. However, it may not produce the desired chamfering width.

In the following, we study how to adjust α so that the center of the cutter rod axis stays within the cylinder (42) to avoid cutter rod interference. The algorithm is described in Algorithm 1. First, we set the initial value for α in (18), where we typically use $\alpha = 1$, then the line equation along $\mathbf{e}$ will be

$$\mathbf{l}(u) = \mathbf{x}_p + u\mathbf{e}, \tag{45}$$

where u is a parameter. There are two intersection points between the line (45) and the closed intersection curve (44) where the intersection point closer to $\mathbf{x}_p$ is the meaningful solution $\mathbf{x}_R$ (see Fig. 11(b)), and the further one is the unwanted solution. The intersection problem can be formulated as a vector equation $\mathbf{l}(u) = \mathbf{C}_R(\theta)$ with two unknowns u and θ (see Fig. 11). The system of equations is overdetermined. Therefore, we first solve the first two equations using Newton's method and select the solution u and θ which satisfy the third. If the correction for Newton's method is large, it is an indication that the problem is highly nonlinear. In such a case, we multiply the correction by a step correction
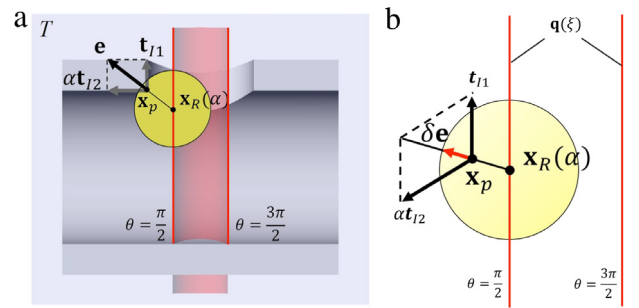
factor μ, where $0 < \mu < 1$. We typically use $\mu = 0.2$. The initial values for u and θ are set equal to $u = r - R_R$ and θ of $\mathbf{x}_p = \mathbf{C}_I(\theta)$, respectively. Since the angle difference along the intersection curve between the meaningful solution and the unwanted solution is about π, it is unlikely to converge to the unwanted solution as long as we use the above initial values together with the damped Newton's method. If we denote the intersection point as $\mathbf{x}_R(\alpha) = (x_R(\alpha), \ y_R(\alpha), \ z_R(\alpha))$, which depends on α, the following condition must be satisfied in order to avoid the cutter rod interference (see Fig. 11(b)):

$$F(\alpha) = (x_p - x_R(\alpha))^2 + (y_p - y_R(\alpha))^2$$
$$+ (z_p - z_R(\alpha))^2 - (R_B - \delta)^2 = 0. \tag{46}$$

With the initial guess of α, (46) is usually not satisfied. Therefore, we adjust α such that $|F(\alpha)|$ becomes smaller than the prescribed tolerance ϵ_α by employing the bisection method [12]. Note that the initial interval for the bisection method is set to satisfy the condition (41); therefore, the solution from Eq. (46) does not violate (41). When the tangent vector (6) is orthogonal to the z-axis, c vanishes and the intersection curve $\mathbf{C}_R(\theta)$ degenerates to two straight lines that are parallel to the z-axis at $\theta = 0, \pi$ or $\theta = \pi/2, 3\pi/2$ as shown in Fig. 12. Let these lines be

$$\mathbf{q}(\xi) = (R_R \cos \theta, \ R_R \sin \theta, \ 0) + \xi(0, \ 0, \ 1). \tag{47}$$

Then, the line–line intersection with (45) can be formulated as follows:

$$(R_R \cos \theta, \ R_R \sin \theta, \ 0) + \xi(0, \ 0, \ 1)$$
$$= (x_p, \ y_p, \ z_p) + u(e_x, \ e_y, \ e_z). \tag{48}$$

The x-component of the vector equation can be used to find u for $\theta = 0$ and π, while the y-component can be used to find u for $\theta = \pi/2, 3\pi/2$. Using this u, the intersection point is evaluated by $\mathbf{x}_R(\alpha) = \mathbf{l}(u)$. The z-component is used to verify the result by obtaining ξ using u, and substituting into (47).

Algorithm 1 Avoidance of cutter rod interference

Input: Initial values α_0, u_0, θ_0, and the tolerance ϵ_α
Output: α_{new}
1: $\alpha_{old} = \alpha_0, u_{old} = u_0, \theta_{old} = \theta_0$
2: **repeat**
3:     $\mathbf{e} = EvaluateCutterVector(\alpha_{old})$
4:     **if** Intersection curve is non-degenerate ($c \neq 0$) **then**
5:         $(u_{new}, \theta_{new}) = ComputeLineEllipseIntersection(\mathbf{e}, u_{old}, \theta_{old})$
6:     **else if** Intersection curve is degenerate ($c = 0$) **then**
7:         $(u_{new}, \theta_{new}) = ComputeLineLineIntersection(\mathbf{e}, u_{old}, \theta_{old})$
8:     **end if**
9:     $\mathbf{x}_R(\alpha_{old}) = EvaluateIntersectionPoint(u_{new}, \theta_{new})$
10:    $\alpha_{new} = UpdateByBisectionMethod(\mathbf{x}_R(\alpha_{old}))$
11:    $\alpha_{old} = \alpha_{new}, u_{old} = u_{new}, \theta_{old} = \theta_{new}$
12: **until** $|F(\alpha_{new})| < \epsilon_\alpha$
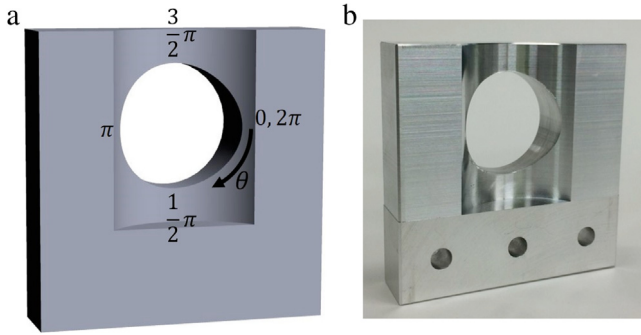
Fig. 13. Pipe models: (a) CAD model. (b) Aluminum model.

Table 1
Experimental conditions.

Exp. No.	2β	Cutter rod interference	ϵ (mm)	# of line segments
1	72°	No	0.02	96
2	93°	Yes	0.01	101
3	93°	No	0.01	101

5. Physical experiments

In this section, we demonstrate the effectiveness of our algorithms by applying them to aluminum pipe models. The experimental setup is only for checking the inner intersection tool path. All of the computations are performed on an Intel Core i7-4770 (3.40 GHz) PC with 8 GB of RAM.

5.1. Experimental setup

Pipes are modeled as shown in Fig. 13(a) for ease of handling and easy measurement, and their geometries are fixed for all of the experiments. The inner diameter of the pipe model and the diameter of the drill are chosen to be $R_I = 36$ mm and $r = 26$ mm, respectively. We use aluminum A5052 for the pipe specimen, as depicted in Fig. 13(b).

The radius of the ball-end cutter is $R_B = 6$ mm, and the rod diameter is $R_{od} = 3.6$ mm. The chamfering width is set to $W = 0.7$ mm. The feed rate and the number of rotations of the cutter are 300 mm/min and 3000 rpm, respectively.

Under these conditions, $1/|\mathbf{k}_e(\theta)|$ $(0 \leq \theta \leq 2\pi)$ is always larger than the radius of the ball-end cutter for $\alpha = 1$ (see Fig. 14(a)), and hence, there is no local interference, as shown in Fig. 14(b), while Fig. 14(c) shows that $-e_z$ is always negative, and therefore, there is no global interference.

We conduct three experiments to remove burrs generated at the pipe hole exit (see Fig. 15(a)). The experimental conditions are presented in Table 1. In Section 5.2, we conduct an experiment (No. 1) where we have no cutter rod interference with $\alpha = 1$. In Section 5.3, we examine the case when the non-knife surface of the cutter interferes with the hole surface using $\alpha = 1$ (No. 2), while in Section 5.4, α is adjusted in some regions so that the cutter rod (non-knife surface) interference is avoided (No. 3).

5.2. Interference-free cutter path with $\alpha = 1$ ($2\beta = 72°$)

Experiment No. 1 is the most typical experiment in pipe deburring where there is no cutter rod interference, even with constant $\alpha = 1$ for $0 \leq \theta \leq 2\pi$. Fig. 15(b) shows a close-up view of the experimental results, which clearly shows the unwanted burrs removed.

5.3. Non-cutting surface interference path with $\alpha = 1$ ($2\beta = 93°$)

If the cutter rod interferes with the hole surface, it may damage the milling machine; therefore, we only test interference with the

Table 2
Measurement of chamfering width.

No.	Projected chamfering width based on computation (mm)	Projected chamfering width based on measurement (mm)
1	0.491	0.485
2	0.495	0.489
3	0.491	0.481

non-knife surface, using a special cutter that has a non-knife angle of $2\beta = 93°$ so that the non-knife surface makes contact with $\mathbf{C}_I(\theta)$. With $\alpha = 1$ $(0 \leq \theta \leq 2\pi)$, the non-knife surface of the cutter interferes with $\mathbf{C}_I(\theta)$, generating scars on the chamfer surface, as shown in Fig. 16. Fig. 14(d) shows that the distance from the center of the sphere exceeds the radius $R_R = r - R_B \sin \beta = 10.824$ mm.

5.4. Interference-free cutter path with $\alpha \neq 1$ ($2\beta = 93°$)

In Section 5.3, we kept $\alpha = 1$ for $0 \leq \theta \leq 2\pi$, and this resulted in the non-knife surface of the cutter interfering with the intersection curve $\mathbf{C}_I(\theta)$. This left scars on the chamfer surface. To avoid such interference, α should be adjusted based on Algorithm 1 such that the distance of the cutter location from the center line $\sqrt{x_{CL}(\theta)^2 + y_{CL}(\theta)^2}$ stays within the interference limit radius R_R, as shown in Fig. 14(e) and (h). Fig. 14(f) and (g) illustrate that even with $\alpha \neq 1$ for some region of $\mathbf{C}_I(\theta)$, $1/|\mathbf{k}_e|$ is always larger than the radius of the ball-end cutter and $-e_z$ is kept negative; hence, there is no local or global interference. Although we conduct the experiment for non-knife surface interference, it is apparent that Algorithm 1 also works to determine the interference-free path with the cutter rod. Fig. 17 confirms that adjusting α avoids the non-cutting surface interference.

5.5. Accuracy of chamfering surface

The accuracy is measured by comparing the top view of the chamfering surface taken by a digital microscope (KEYENCE VHX-900), with that of the computing models overlaid on the chamfered surface, as shown in Fig. 18. Table 2 compares the projected chamfering width (top view) of the computational model and the measurements at three different locations. The overlaid image in Fig. 18 and Table 2 demonstrate that the edge curve is accurately chamfered.

5.6. Comparison with hand deburring

The computational time for the cutter path generation, constant feed rate of the milling machine, and the time for deburring are listed in Table 3. Because the cutter rod (non-knife surface) interference is involved in the experiment, for safety, we reduce the feed rate to one sixth of the value used in real operations. In real operations, the feed rate is typically 1800 mm/min, and the deburring operation takes only 2.4 s. According to Uchida [13], burrs become larger as r/R_I approaches one, and hand-held deburring tools are required to remove burrs. Therefore, it takes about 30 s on average to complete the finishing operations. In summary, the deburring time is about 12 times faster than that of hand deburring, and in terms of the chamfering width, the quality is much better. Furthermore, our method can significantly reduce the labor cost. Fig. 19 shows a typical result obtained for hand-held deburring, which clearly shows that the chamfering width is not constant; moreover, unwanted scars are generated by the worker.
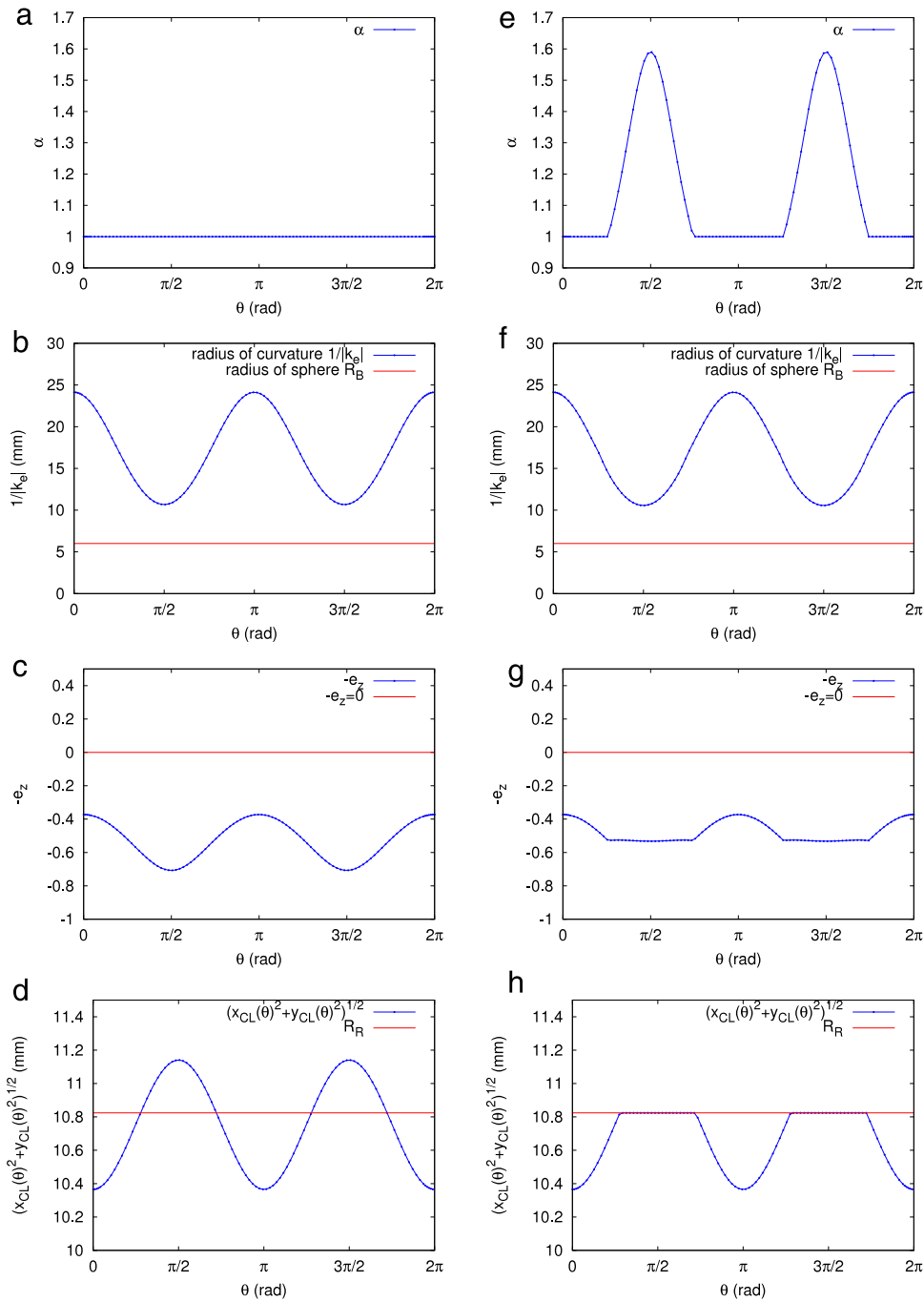
Fig. 14. Computational results. Figures in the left-hand side column are the results for $\alpha = 1$ for $(0 \leq \theta \leq 2\pi)$, while those in the right-hand side column are the results for $\alpha \neq 1$. From top to bottom, α distribution, local interference check, global interference check, cutter location distance from the center line $\sqrt{x_{CL}(\theta)^2 + y_{CL}(\theta)^2}$.

6. Conclusion

In this paper, we introduced an interference-free automatic tool path generation method for a ball-end cutter to remove burrs resulting from the drilling of a circular pipe with constant chamfer based on the differential geometry of cylinder-to-pipe intersection curves.

The advantages of our algorithm are as follows:

- An efficient and accurate automatic collision-free tool path is generated.
- Burrs are removed with constant chamfering. Furthermore, the cutter vector divides the cross section of the chamfered surface into two equi-length circular arcs.

Table 3
Experimental results.

	Comp. time (s)	Feed rate (mm/min)	Deburring time (s)
Exp. 1	0.046	300	14.3
Exp. 2	0.047	300	14.3
Exp. 3	0.062	300	14.3
Real operations	0.046	1800	2.4
Hand deburring	–	–	30.0

- The parameter values at the sequence of reference points are determined such that the feedrate of the machine operates as a function of the distance along the tool path.
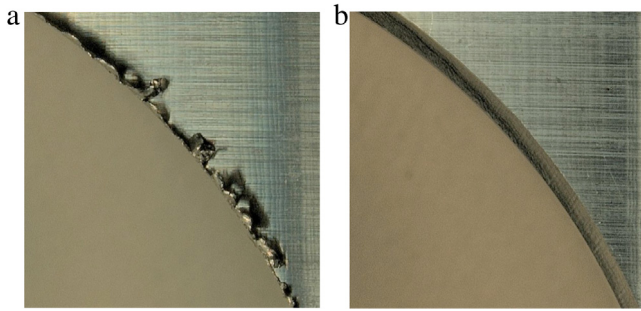
Fig. 15. (a) Burrs generated at the hole exit ($3\pi/2 < \theta < 2\pi$). (b) The experimental results of Exp. No. 1, which clearly show that the unwanted burrs are removed with constant chamfering at the edge. The chamfering width does not appear to be constant, but this is because of the view point of the image.
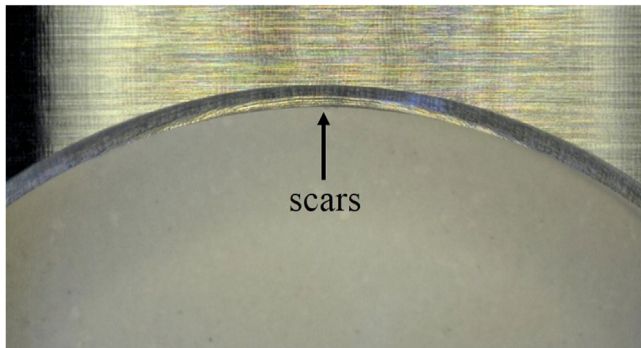
Fig. 16. Scars are generated on the chamfered surface.
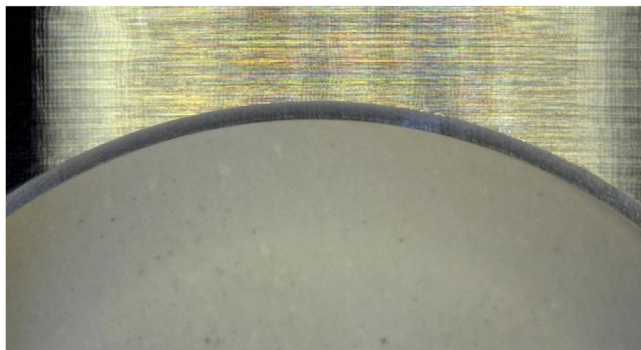
Fig. 17. By adjusting α, non-cutting surface interference is avoided.

We provided an outline of the concept of deburring the edges resulting from drilling a circular hole in a circular pipe. However, there are several possibilities for extensions of our algorithm, two of which are:

- The algorithm can be extended to automatically generate a tool path for an inclined hole, and for a hole with eccentricity.
- The algorithm can be extended to the deburring of drilled holes of cone pipes with constant chamfering.

Appendix A. Supplementary data

Supplementary material related to this article can be found online at http://dx.doi.org/10.1016/j.cad.2016.04.008.
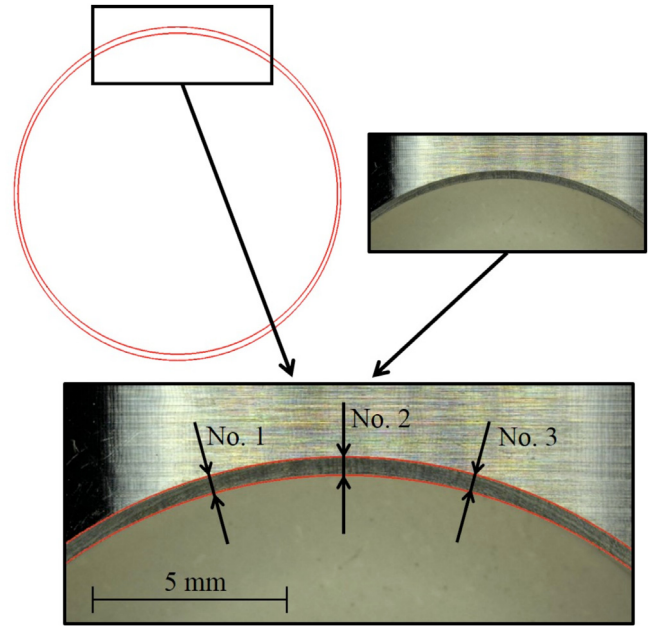
Fig. 18. Accuracy of the chamfering surface. Top left: Computer model of chamfering surface. Top right: Deburred aluminum model. Bottom: Chamfering surface is precisely overlaid on the deburred aluminum model.
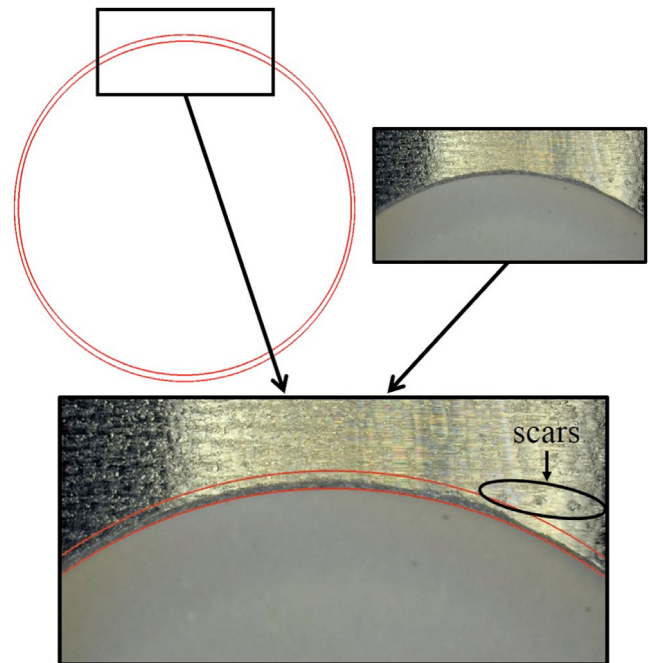
Fig. 19. The result of hand deburring. Compared with Fig. 18, the quality of chamfering is not comparable in terms of chamfer width and appearance.

References

[1] Ramachandran N, Pande SS, Ramakrishnan N. The role of deburring in manufacturing: A state-of-the-art survey. J Mater Process Technol 1994;44(1): 1–13.
[2] Gillespie LK. Deburring precision miniature parts. Precis. Eng. 1979;1(4): 189–98.
[3] Liao L, Xi FJ, Liu K. Modeling and control of automated polishing/deburring process using a dual-purpose compliant toolhead. Int J Mach Tools Manuf 2008;48(12):1454–63.
[4] Song HC, Song JB. Precision robotic deburring based on force control for arbitrarily shaped workpiece using cad model matching. Int. J. Precis. Eng. Manuf. 2013;14(1):85–91.
[5] Ye X, Maekawa T. Differential geometry of intersection curves of two surfaces. Comput Aided Geom Design 1999;16(8):767–88.

[6] Sarraga RF. Algebraic methods for intersections of quadric surfaces in gmsolid. Comput. Vis. Graph. Image Process. 1983;22(2):222–38.

[7] Maekawa T. An overview of offset curves and surfaces. Comput Aided Des 1999;31(3):165–73.

[8] Patrikalakis NM, Maekawa T. Shape interrogation for computer aided design and manufacturing. Heidelberg: Springer-Verlag; 2002.

[9] Faux ID, Pratt MJ. Computational geometry for design and manufacture. Chichester, England: Ellis Horwood; 1981.

[10] Yang DCH, Kong T. Parametric interpolator versus linear interpolator for precision cnc machining. Comput Aided Des 1994;26(3):225–34.

[11] Farouki RT, Shah S. Real-time CNC interpolators for pythagorean-hodograph curves. Comput Aided Geom Design 1996;13(7):583–600.

[12] Press WH, Teukolsky SA, Vetterling WT, Flannery BP. Numerical recipes 3rd edition: The art of scientific computing. third ed. New York, NY, USA: Cambridge University Press; 2007.

[13] Uchida K. Private communication, November 2015.